A&A, 712, A72 (2026)
https://doi.org/10.1051/0004-6361/202660671
© The Authors 2026

Astronomy & Astrophysics

Kinematic detection of dusty outflows from active galactic nuclei: Polycyclic aromatic hydrocarbon kinematics of type 2 quasars with JWST/MIRI spectroscopy

Fergus R. Donnan[1,⋆], Cristina Ramos Almeida[2,3], Omaira González Martín[4], Karin Sandstrom[1], Anelise Audibert[2,3], Marina Bianchin[2,3], Miguel Pereira-Santaella[5], and Ismael García-Bernete[6]

[1] Department of Astrophysics, University of California San Diego, 9500 Gilman Drive, San Diego, CA 92093, USA
[2] Instituto de Astrofísica de Canarias, Calle Vía Láctea, s/n, 38205 La Laguna, Tenerife, Spain
[3] Departamento de Astrofísica, Universidad de La Laguna, 38206 La Laguna, Tenerife, Spain
[4] Instituto de Radioastronomía y Astrofísica (IRyA), Universidad Nacional Autónoma de México, Morelia, Michoacán, Mexico
[5] Instituto de Física Fundamental, CSIC, Calle Serrano 123, 28006 Madrid, Spain
[6] Centro de Astrobiología (CAB), CSIC–INTA, Camino Bajo del Castillo s/n, 28692 Villanueva de la Cañada, Madrid, Spain

Received 28 April 2026 / Accepted 26 June 2026

ABSTRACT

Context. Active galactic nuclei (AGN) are thought to have dusty outflows, but unlike in the gas phase, it is challenging to measure the kinematics of dust.
Aims. We present the detection and analysis of the kinematics of dust in five type 2 quasars at $z \sim 0.1$ from the Quasar Feedback (QSOFEED) sample observed with JWST/MIRI spectroscopy.
Methods. We used principal component analysis tomography to produce velocity maps of polycyclic aromatic hydrocarbon (PAH) features, which are the smallest carbonaceous dust particles. We were then able to compare velocity maps of the PAHs with emission lines of ionised and molecular gas.
Results. We produced velocity maps of the 11.3 μm PAH feature, which traces large and neutral PAHs, for three out of the five objects, where all three show an outflow in the PAH kinematics. This becomes particularly clear after we subtracted disk kinematics, where the H_2 rotational transitions also show residuals consistent with an outflow. Compared to previous work with Seyfert galaxies, this work suggests that dusty outflows are more common at higher Eddington ratios, $\lambda_{\rm Edd} \gtrsim 0.1$, in agreement with previous suggestions, although the sample size is small. We were unable to produce velocity maps for the 6.2 μm PAH, which traces ionised PAHs, potentially due to differences in the intrinsic profile and/or suppression of the feature in AGN, which was seen previously in Seyfert galaxies. This reflects studies of PAH band ratios where AGN outflows have more neutral PAHs.
Conclusions. This work demonstrates that dusty outflows may be common, particularly at high Eddington ratios, and it therefore plays a key role in the evolution and life cycle of AGN.

Key words. ISM: general – ISM: jets and outflows – galaxies: active

1. Introduction

Active galactic nuclei (AGN) are known affect their host galaxy through feedback processes, and they thus play a pivotal role in the evolution of galaxies (e.g. Kormendy & Ho 2013; Heckman & Best 2014). Because the majority of AGN are obscured by dust (e.g. Ramos Almeida & Ricci 2017; Hickox & Alexander 2018; Boorman et al. 2025), many key questions exist about the nature and lifetime of dust around AGN. A typical picture of galaxy evolution suggests that as AGN activity is triggered, such as through galaxy mergers, a dust-obscured phase of rapid supermassive black hole growth occurs (e.g. Sanders et al. 1988; Hopkins et al. 2008; Ricci et al. 2022). The subsequent radiation field of the accretion disk is then able to clear the obscuring dust, resulting in dusty outflows (e.g. Fabian et al. 2008; Ishibashi & Fabian 2018; Arakawa et al. 2022) and leading to AGN that can be observed in the optical. Moreover, the relatively recent discovery of numerous little red dots (e.g. Hviding et al. 2025; Kocevski et al. 2025; Rusakov et al. 2026; Pérez-González et al. 2026), which show high column density gas obscuring a supermassive black hole, but little dust (Barro et al. 2025; Casey et al. 2024; Chen et al. 2025; Delvecchio et al. 2025) despite the presence of metal emission lines (e.g. Matthee et al. 2024), adds to this story, further suggesting that AGN may clear their dust (e.g. Matthee et al. 2026). Therefore, the expulsion of dust through AGN-driven winds is a key process for understanding how AGN evolve and inject material into the interstellar medium.

Extended dust in the polar axis of AGN were detected via mid-infrared imaging (Braatz et al. 1993; Bock et al. 2000; Radomski et al. 2002, 2008; Packham et al. 2005; Reunanen et al. 2010; Asmus et al. 2014, 2016; García-Bernete et al. 2016; Asmus 2019; Stalevski et al. 2017; Haidar et al. 2024, 2026; Campbell et al. 2025) and with infrared interferometry in particular, providing the high angular resolution needed to image AGN tori, revealing polar structure perpendicular to the tori (Raban et al. 2009; Hönig et al. 2012, 2013; López-Gonzaga et al. 2014; Tristram et al. 2014; López-Gonzaga et al. 2016; Leftley et al. 2018; Isbell et al. 2022; Gámez Rosas et al. 2022). The first kinematic

⋆ Corresponding author: fdonnan@ucsd.edu

Open Access article, published by EDP Sciences, under the terms of the Creative Commons Attribution License (https://creativecommons.org/licenses/by/4.0), which permits unrestricted use, distribution, and reproduction in any medium, provided the original work is properly cited.
This article is published in open access under the Subscribe to Open model. Subscribe to A&A to support open access publication.

Table 1. Objects from the QSOFEED sample observed with JWST/MIRI MRS.

SDSS ID	Short ID	RA	Dec	z	$\log L_{\rm bol}$ erg s^{-1}	$\log \lambda_{\rm Edd}$	$\log M_{\rm BH}$ $M_\odot$	$\log N_H$ cm^{-2}	i °	PA °
(1)	(2)	(3)	(4)	(5)	(6)	(7)	(8)	(9)	(10)	(11)
J101043.36+061201.4	J1010	10:10:43.36	+06:12:01.4	0.0977	45.6	-0.8 ± 0.8	8.4 ± 0.8	22.3	37 ± 1	287 ± 8
J110012.39+084616.3	J1100	11:00:12.39	+08:46:16.3	0.1004	45.9	0.0 ± 0.5	7.8 ± 0.4	22.6	38 ± 1	68 ± 3
J135646.10+102609.0	J1356	13:56:46.10	+10:26:09.0	0.1232	45.5	-1.0 ± 0.4	8.6 ± 0.3	23.0	54 ± 1	107 ± 11
J143029.88+133912.0	J1430	14:30:29.88	+13:39:12.0	0.0851	45.8	-0.4 ± 0.4	8.2 ± 0.4	22.9	38 ± 2	27 ± 3
J150904.22+043441.8	J1509	15:09:04.22	+04:34:41.8	0.1115	46.0	-0.2 ± 0.8	8.3 ± 0.8	23.1	43 ± 1	266 ± 4

Notes. (1) SDSS source ID. (2) Short ID. (3) Right ascension. (4) Declination. (5) Redshift. (6) AGN bolometric luminosity from extinction-corrected [O III] luminosities, from Ramos Almeida et al. (2026). (7) Eddington ratio from Kong & Ho (2018). (8) Black hole mass from Kong & Ho (2018). (9) Column density from CO (Ramos Almeida et al. 2026). (10) Disk inclination. (11) Disk position angle. The disk inclination and position angles correspond to those derived from modelling of CO(2–1) data from Audibert et al. (2025), except in the case of J1430 (PA=3 ± 1 in Audibert et al. 2025), where the position angle was inferred from the [NeII] velocity map presented here.

evidence of dusty outflows from AGN was presented in Donnan et al. (2026) through the measurement of the velocity of polycyclic aromatic hydrocarbon (PAH) features in the infrared.

PAHs are the smallest carbonaceous dust grains, consisting of aromatic rings of carbon with hydrogen bonds, and they make up ∼1%–5% of the mass of dust in galaxies (e.g. Draine & Li 2007) but can contribute up to 20% of the luminosity of dust grains (e.g. Smith et al. 2007) in metal-rich galaxies. After excitation from a UV photon, these molecules relax, where the C–C and C–H bonds bend and stretch at various frequencies, giving rise to broad emission features in the infrared (3–17 μm; e.g. Tielens 2008; Li 2020). Unlike the thermal continuum from stochastically heated dust grains, which dominate the continuum emission in the infrared, it is possible to measure the Doppler velocity shifts of PAH features, although there are significant challenges. Typically, PAHs are fitted using an integrated spectrum such as PAHFIT (Smith et al. 2007), CAFE (Marshall et al. 2007; Diaz-Santos et al. 2025), or SPIRIT (Donnan et al. 2024a) due to their broad profiles.

PAHs are typically observed to have a lower equivalent width in AGN (e.g. Armus et al. 2007; Spoon et al. 2007; Alonso-Herrero et al. 2014; Ramos Almeida et al. 2014; Donnelly et al. 2024; Lai et al. 2023; Ramos Almeida et al. 2023; García-Bernete et al. 2024) because of the strong dust continuum from the torus and/or destruction of the PAHs through processes such as photo-destruction or shocks (e.g. Siebenmorgen et al. 2004; García-Bernete et al. 2022a, 2024; Zhang & Ho 2023; Zhang et al. 2024a, 2026). The PAH band ratios in AGN outflows show more neutral and larger PAHs, consistent with the idea of preferential destruction of small and ionised PAHs (e.g. García-Bernete et al. 2022a, 2024).

There are two main challenges to measuring PAH kinematics. First, the features are significantly broader than any velocity shift, and second, the shape of the intrinsic feature profile is not well defined and can vary depending on the excitation conditions and properties of the PAH molecules (e.g. Peeters et al. 2002; Candian & Sarre 2015; Shannon & Boersma 2019; Canelo et al. 2026). For these two reasons, traditional methods of measuring kinematics such as modelling each spaxel and fitting for a velocity are not feasible. Instead, Donnan et al. (2024b) showed how principal component analysis (PCA) tomography (Steiner et al. 2009) can be used to measure PAH kinematics. They presented the first velocity maps of PAH features. This work was followed by Donnan et al. (2026), where the first kinematic detection of outflowing dust from AGN was presented.

The sample studied in Donnan et al. (2026) was restricted to Seyfert galaxies with fairly low Eddington ratios ($\log \lambda_{\rm Edd} \lesssim -1.5$) and AGN luminosities ($\log L_{\rm bol} \lesssim 44$ erg s^{-1}). In this work, we apply the same techniques to a sample of five optically selected type 2 quasars (QSO2s) from the Quasar Feedback (QSOFEED) sample (Ramos Almeida et al. 2022; Pierce et al. 2023; Bessiere et al. 2024). These QSO2s occupy a parameter space of higher AGN luminosity and higher Eddington ratio ($\log L_{\rm bol} \gtrsim 45.5$ erg s^{-1} and $\log \lambda_{\rm Edd} \gtrsim -1.0$; Ramos Almeida et al. 2025, 2026). Unlike the majority of Seyfert galaxies, which are found in the permitted region of the column density–Eddington ratio diagram (Fabian et al. 2008; Ricci et al. 2017), the five QSO2s are in either the blowout or polar dusty winds regions, indicating that they must be actively clearing gas and dust from their nuclear regions (Ramos Almeida et al. 2026). Incidentally, the Ramos Almeida et al. (2026) successfully reproduced the JWST MIRI nuclear spectrum of one of them with the CAT-3D wind model of Hönig & Kishimoto (2017), which models a clumpy torus with a dusty wind component. Therefore, these targets are ideal candidates for studying their PAH kinematics and comparing them with the results found for lower-luminosity AGN (Donnan et al. 2026).

The paper is structured as follows. In Sect. 2, we describe the QSOFEED sample and the MIRI MRS observations with JWST. In Sect. 3, we describe the method of PCA tomography and kinematic modelling of the disk kinematics. In Sect. 4, we present velocity maps for each target. Finally, in Sect. 5, we discuss our results. Throughout this work, we assume a Λ cold dark matter cosmology with $H_0 = 70$ km s^{-1} Mpc^{-1}, $\Omega_m = 0.27$, and $\Omega_\Lambda = 0.73$.

2. Sample, observations, and data reduction

We used MIRI MRS observations from the JWST general observer program 3655 (PI: Ramos Almeida; MAST doi:10.17909/8w9h-re72). Five optically selected QSO2s with redshifts $0.09 \leq z \leq 0.12$, AGN luminosities of $\log L_{\rm bol} = 45.5$–46.0 erg s^{-1}, and stellar masses of $\log M_* = 10.9$-11.3 $M_\odot$ were observed as part of this programme (see Table 1). They are representative of the gas-rich QSO2s in the QSOFEED sample, with total molecular gas masses of $M_{H_2}=4-18\times10^9$ $M_\odot$ and evidence of cold molecular outflows detected from Atacama Large Millimeter Array (ALMA) CO observations (Ramos Almeida et al. 2022; Audibert et al. 2025). They also have some of

the most extreme ionised gas kinematics within the QSOFEED sample (Bessiere et al. 2024; Speranza et al. 2024).

The mid-infrared nuclear spectra of the five QSO2s, obtained from the JWST MIRI observations used here, were first presented in Ramos Almeida et al. (2025, 2026). They revealed different continuum shapes and silicate feature strengths, including emission features, even though they are obscured quasars. Their [NeV]/[NeII] ratios range from 0.1 to 2.1 and [NeIII]/[NeII] from 1.0 to 3.5, indicating different coronal line and ionising continuum strengths. The equivalent widths of the PAH bands range from less than 0.002 to 0.075 μm, from which Ramos Almeida et al. (2025) measured nuclear star formation rates of ≤3–7 $M_\odot$ yr^{-1} and a higher fraction of neutral PAHs over the ionised ones.

The MIRI MRS observations were made from May 2024 to January 2025 using a four- and two-point dither sequence for the target and background observations, respectively (we refer to Ramos Almeida et al. (2025) for details on the observations). The data reduction was made as described in González-Martín et al. (2025), using version 1.14.1 of the JWST pipeline (Bushouse et al. 2024). After the data cubes were reduced, we subtracted the unresolved point spread function (PSF) from them using the tool *MRSPSFisol* (González-Martín et al. 2025). This step is key to studying the underlying extended emission of the QSO2s, as their high luminosities can result in a very strong point source from the hot dust continuum of the torus. The analysis presented in the following sections was conducted using the PSF-subtracted cubes, but all the velocity maps presented here were also created with the original non-PSF-subtracted ones for comparison. The original cubes produce much noisier maps, but are generally similar. This is likely because the PCA detects small wiggles and artefacts as bright features because the PSF is relatively bright compared to the circumnuclear emission. For the PSF-subtracted cubes, the PCA detects any artefacts well, resulting in a clean velocity component (see Sect. 3).

3. Methods

3.1. PCA tomography

The application of PCA to astronomical integral field unit data cubes was first presented by Steiner et al. (2009), who used PCA tomography to linearly decompose the data cube into orthogonal components. These components consist of specific spectral features that have some spatial distribution, ordered such that the first principal component contains the greatest variance in the data, with subsequent components containing progressively less variance. Typically, higher-order components contain only noise.

PCA tomography was first shown to be able to measure the kinematics of PAH features by Donnan et al. (2024b), where the first principal component typically contains the rest-frame emission and the second component contains the velocity information. Before applying the PCA decomposition to the data cube of a given emission feature, we first subtracted a local continuum around the feature. This helped us to isolate the emission feature as the continuum can have a different spatial distribution to the emission feature and can thus confuse the PCA decomposition, where it instead identifies regions of continuum versus emission feature rather than kinematics. We constructed a local continuum by masking the emission feature and fitting a straight line in f_ν to the 15 wavelength channels of either side of the sub-cube. This is an approximate continuum and did remove some of the PAH flux in the wings. However, as we are interested in the kinematics and not the fluxes of the PAH features, this simple continuum is sufficient. We explore the continuum subtraction further in Appendix B. The continua used for the 6.2 μm and 11.3 μm PAH features are shown in Fig. 1.

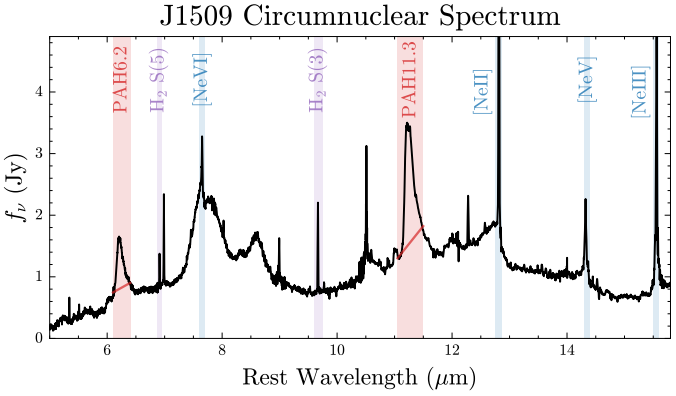


Fig. 1. Circumnuclear spectrum of J1509, extracted through a 2″ radius aperture from the PSF-subtracted cubes. We highlight the emission features we analysed. The local continua used for the PAH features are also shown.

After continuum subtraction, the subtracted cube had the form $\mathbf{I}_{x,y,\lambda}$. We applied smoothing using a Gaussian kernel with $\sigma = 1$ pixel and then masked pixels with a low signal-to-noise ratio following the process described in Donnan et al. (2026). The cube was then collapsed into two dimensions, where the spatial dimensions, x, y were transformed by

$$\beta = \mu(x - 1) + y, \tag{1}$$

where there are $\mu \times \nu$ total spatial pixels, resulting in the data having the form of a 2D array, $\mathbf{I}_{\beta,\lambda}$. The PCA was applied to this array, where

$$\mathbf{T}_{\beta,k} = \mathbf{I}_{\beta,\lambda} \cdot \mathbf{E}_{\lambda,k}, \tag{2}$$

where $\mathbf{T}_{\beta,k}$ are the tomograms of each principal component, k, which is the spatial distribution of a given spectral feature, $\mathbf{E}_{\lambda,k}$, which are known as eigenspectra.

We constructed a velocity map from the PCA decomposition by taking the eigenspectrum of the first principal component as the rest-frame emission profile and measuring the wavelength shift and thus velocity required to reproduce the spectral profile of each spaxel on the reconstructed data cube using the first four principal components (higher-order components are dominated by noise, containing ≲1% of the variance; Donnan et al. 2024b). More details of this process can be found in Donnan et al. (2026). To produce velocity error maps, we repeated the process 50 times, resampling the data each time from the error bars of the data cube, and took the standard deviation of the 50 samples to obtain an error estimate of the velocity.

We demonstrate the PCA decomposition as applied to the 11.3 μm PAH for J1509 in Fig. 2. The velocity information is contained in the third principal component, where the second detects artefacts from the PSF subtraction. We verified that we traced the velocity by inspecting the shape of the third principal component, which should match the derivative of the first component in the case of a Doppler shift. This is because PCA is a linear decomposition, and we can write a Doppler shift as a linear function after a Taylor expansion,

$$f_{\rm obs}(\lambda) \approx f_{\rm rest}(\lambda) + \frac{v}{c}\frac{df_{\rm rest}}{d\lambda}\lambda \approx a_i^{(1)}\phi_1(\lambda) + a_i^{(2)}\phi_2(\lambda) + ..., \tag{3}$$

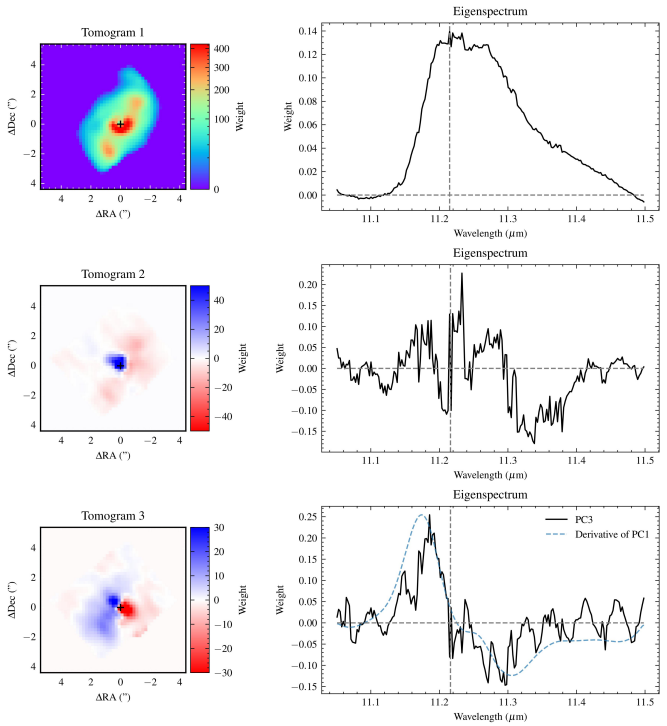


Fig. 2. PCA decomposition of the 11.3 PAH feature for J1509. *Right panels*: eigenspectra of each component. *Left panels*: tomograms that describe how the eigenspectra map onto the spatial axes. The dashed blue line shows the derivative of the eigenspectrum of the first principal component, which is expected to match the eigenspectrum of the component containing velocity information, in this case, component 3. The second component detects artefacts in the nucleus due to the PSF subtraction. The vertical dashed line shows where the third eigenspectrum crosses from positive to negative.

where $f_{\rm obs}$ is the observed emission feature at velocity, v, where $f_{\rm rest}$ is the rest-frame feature. The left-hand side is the PCA decomposition, where $a_i^{(j)}$ is the tomogram of component j, and $\phi_j(\lambda)$ is the corresponding eigenspectrum. This shows that we expect the first component to be rest-frame emission and a higher-order component to contain the velocity information with an eigenspectrum proportional to the derivative of the rest frame profile. This is indeed what we observe in Fig. 2, where the PSF artefacts add into the data linearly (as PSF subtraction is a linear process, this makes sense) in addition to the Doppler shift. The artefacts appear as component 2 rather than 3 because they contain more variance in the original data than the velocity (this is shown in Fig. 2, where tomogram 2 had higher weights than tomogram 3).

We applied the PCA decomposition and constructed velocity maps for ionised and molecular gas emission lines as well as the 6.2 μm and 11.3 μm PAH features as these features are sufficiently bright and narrow enough. For the ionised gas, we used the [NeII] (12.81 μm, 41 eV), [NeV] (14.32 μm, 126 eV), and [NeVI] (7.65 μm, 158 eV) lines to trace the low and highly ionised gas respectively. For the molecular gas, we used the H_2 S(1) (17.03 μm) and the H_2 S(3) (9.66 μm) rotational transitions of molecular hydrogen. These emission features are highlighted in Fig. 1.

3.2. Disk modelling

The position angle (PA) and inclination of the circumnuclear disk was well constrained for each of the five quasars by fitting a disk model to CO observations (Ramos Almeida et al. 2022; Audibert et al. 2025). This allowed us to model and subtract the disk kinematics to reveal any non-circular motions due to inflowing or outflowing material (e.g. Davies et al. 2024; Donnan et al. 2026).

We followed the disk modelling presented in Veenema et al. (2025) and Donnan et al. (2026), where we fitted the 2D velocity map of each emission feature with a fixed inclination, i, and position angle, ϕ, while fitting for a radial dependent rotation curve, $V(R)$, parametrised by a tanh function that allows the rotation curve to rise steeply where $R < R_{\rm turn}$ and flatten at $R > R_{\rm turn}$. The rotation curve has the form

$$V(R) = V_{\rm max} \tanh\left(\frac{R}{R_{\rm turn}}\right), \tag{4}$$

where the $V_{\rm max}$ and $R_{\rm turn}$ are free parameters. The observed velocity, $V_{\rm obs}(x, y)$, of each spaxel (x, y) is therefore

$$V_{\rm obs}(x, y) = V_{\rm sys} + V(R)\, \sin i\, \cos\theta, \tag{5}$$

where $V(R)$ is the velocity of each ring at radius R, and $V_{\rm sys}$ is the systemic velocity. The radius, R, is the intrinsic deprojected radius that relates to the coordinates of each spaxel (x, y) via

$$x' = x\cos\phi + y\sin\phi,$$
$$y' = -x\sin\phi + y\cos\phi,$$
$$R = \sqrt{x'^2 + \left(\frac{y'}{\cos i}\right)^2},$$
$$\cos\theta = \frac{x'}{R}.$$

We fitted the 2D disk model to the velocity map using Markov chain Monte Carlo sampling from NUMPYRO (Phan et al. 2019). We fixed the inclination and position angle to the values shown in Table 1, which were measured from CO data in Audibert et al. (2025). We fixed the orientation of the disk as it is difficult to constrain from a velocity map alone if there are multiple components such as outflows and bars. We did this for each galaxy, but as we discuss in Sect. 4, only three of the five targets show a reliable detection of kinematics in the PAH features, namely J1100, J1430, and J1509, likely due to the low signal-to-noise ratio in the two remaining targets.

4. Results

4.1. Velocity maps

We present velocity maps for each for the five QSO2s in Fig. 3 of ionised gas, molecular gas, and the 11.3 μm PAH. We also show the position angle of the large-scale galaxy disk as inferred from CO data (Ramos Almeida et al. 2022; Audibert et al. 2025). We find clear differences in the position angle of the kinematic axis for different features, likely reflecting different contributions of outflowing, inflowing and rotating material. In the following sections, we discuss the kinematics of the ionised, molecular, and dust phases for the five objects.

4.1.1. Ionised gas

The kinematics of the low-ionisation potential [NeII] line trace the gas disk well, matching the position angle of the CO data, except in the case of J1430 (see Table 1). The high-ionisation

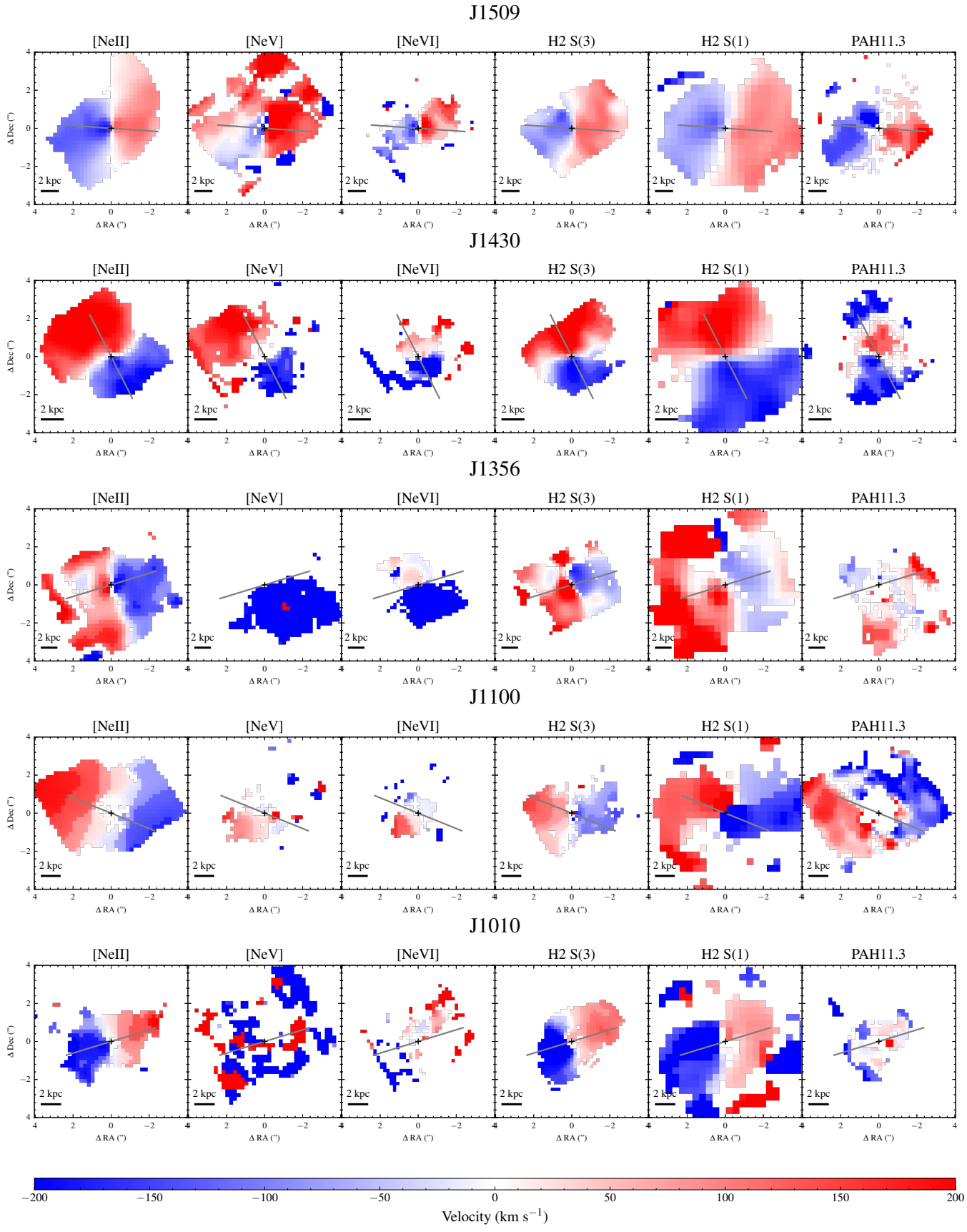


Fig. 3. Velocity maps of each spectral feature for each galaxy derived from the PCA decomposition. We only show spaxels where the velocity was measured to >1σ. Each panel has the same velocity scale from –200 to 200 km s^{-1}. The solid grey line shows the direction of the major axis of the galaxy disk for each galaxy and can be found in Table 1.

[NeV] and [NeVI] lines also predominantly trace the disk kinematics, with a kinematic axis consistent with [NeII], unlike in Seyfert galaxies (e.g. Hermosa Muñoz et al. 2024; Zhang et al. 2024b; Veenema et al. 2026; Donnan et al. 2026), where there is a clear separation of outflow, traced by [NeVI], and disk, traced by [NeII]. This is particularly clear for J1509. J1100 is an exception and does show the typical behaviour, where [NeV] and [NeVI] trace a different velocity structure than [NeII].

The velocity maps of [NeV] and [NeVI] show disk kinematics in the QSO2s. This suggests that the AGN, of higher luminosity than the Seyfert galaxies, has ionised all the surrounding gas (Bianchin et al. 2026). From spatially resolved Baldwin, Phillips, and Terlevich (BPT) diagrams involving optical emission lines detected with VLT/MUSE, Venturi et al. (2023) and Ulivi et al. (2024) showed that the bulk of the line-emitting gas in QSO2s, including J1010, J1100, and J1430, is photoionised by the AGN. In contrast, the disks of Seyfert galaxies include a significant fraction of the gas, which is sometimes dominant and is ionised by star formation (Mingozzi et al. 2019).

As mentioned in Sect. 2, the five QSO2s we studied have ionised and molecular outflows that have been characterised using different methods (Ramos Almeida et al. 2017, 2019, 2022; Speranza et al. 2024; Audibert et al. 2025). We show the velocity dispersion for [NeV] in J1509 and J1430 in Fig. 5. We created this map by fitting a Gaussian line profile to each spaxel and fitting for the width of the Gaussian as parametrised by the velocity dispersion, σ, and the line spread function of MIRI MRS at the observed wavelength. The [NeV] emission shows enhanced velocity dispersion along the outflow for J1509 and J1430, while the dispersion is low across the disk. Therefore, the outflow is indeed present in the highly ionised gas, but only apparent in the velocity dispersion for J1509 and J1430[1]. This suggests that the ionised gas, unlike the molecular and dust phases, is highly turbulent and is thus disturbed by the outflow, as previously shown from a non-parametric analysis of the optical [OIII] emission of J1509 (Bessiere et al. 2024; Speranza et al. 2024). For J1100, the outflow can be seen in the velocity map, where the position angle of the kinematics is different for high-ionisation lines compared to the low-ionisation lines (such as [NeII]).

4.1.2. Molecular gas

The velocity maps of the molecular gas as traced by the rotational H_2 S(5), S(3), and S(1) lines broadly trace rotation with a position angle consistent with the galaxy disk. From these maps alone, any outflow contribution is not immediately clear. However, we investigate the presence of the warm molecular outflows further in Sect. 4.2. J1100 is an exception, where the higher J transitions such as S(3) are more similar to the high-ionisation lines and the 11.3 μm PAH.

4.1.3. PAHs

Out of the five objects, J1509, J1430, and J1100 show coherent kinematic structures in the 11.3 μm PAH feature. In all three cases, there are clear redshifted and blueshifted structures with different orientation that the disk, which might suggest the presence of the outflow in the PAH velocity maps. We show the profile of the 11.3 μm PAH feature for J1509 in Fig. 4, where we show the rest-frame profile and the profiles of the redshifted and blueshifted lobes.

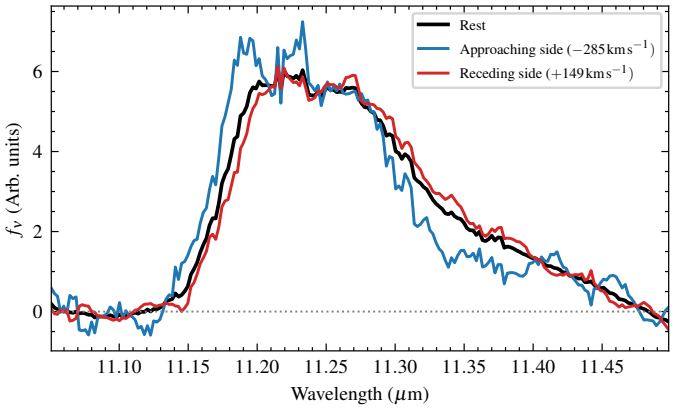


Fig. 4. Profiles of the 11.3 μm PAH feature of the rest-frame emission (eigenspectrum of the first component), the blue- and redshifted sides of the outflow structure with velocities displayed in the legend. These are the average profiles within 0.4″ radius apertures.

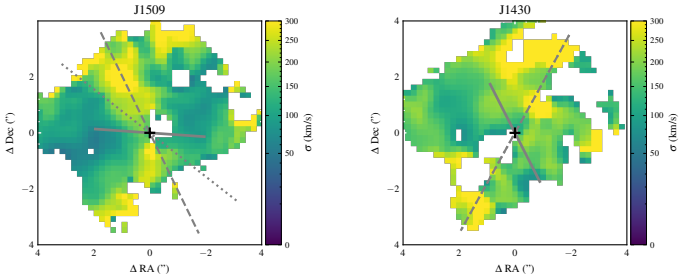


Fig. 5. Velocity dispersion, σ, of [NeV] for J1509 and J1430, as measured by fitting a Gaussian line profiles to each spaxel. The AGN position is shown with the black cross, and the position angle of the galaxy disk is shown with the solid grey line. The dotted and dashed lines show the position angles of the PAH outflow and H_2 outflow for J1509 (see Fig. 6 for reference). For J1430, the PAH and H_2 outflow are shown by the dashed line. The solid grey line shows the position angle of the disk.

Due to the location of the 11.3 μm PAH feature within the 9.7 μm silicate feature, we considered whether extinction is an issue that might cause erroneous velocity measurements. If there is a strong change in extinction spatially, in regions of higher extinction the short-wavelength side of the feature is suppressed relative to the longer wavelength side, mimicking a redshift. This can result in redder velocities when the extinction is high $\Delta\tau_{9.7} \gtrsim 1$. While the nuclear spectra of our sample can show deep silicate features (Ramos Almeida et al. 2025), the circumnuclear emission in our PSF-subtracted cubes does not show high levels of extinction (see Fig. 1). Moreover, fitting the circumnuclear spectra with SPIRIT (Donnan et al. 2024a)[2] yielded low extinction measurements, with an H_2 extinction of $\tau_{9.7} \sim 0.4$ for J1509. Therefore, we conclude that extinction does not affect our measured velocities in any significant way.

As mentioned above, only J1100 shows [NeV] and [NeVI] velocity maps that are clearly distinct from the disk rotation. The 11.3 μm PAH velocity map indeed resembles the [NeV] much more than [NeII] in this target, suggesting that the 11.3 μm PAH is dominated by the outflow in this source. We explore the PAH

[1] We note that the ionised outflow in these QSO2s is detected in velocity and velocity dispersion using parametric and non-parametric methods to fit the emission lines (Ramos Almeida et al. 2019; Speranza et al. 2024).

[2] https://github.com/FergusDonnan/SPIRIT

velocity maps further, after subtracting the disk kinematics, in Sect. 4.2.

We find it challenging to construct velocity maps for the 6.2 μm PAH because the signal-to-noise ratio of this feature is low. The only target with a sufficient signal-to-noise ratio to detect a coherent signal in the second principal component was J1509. In this target, however, the PCA detected a different intrinsic profile rather than a Doppler shift. This was also found in Donnan et al. (2026), and so the PCA detects differences in the intrinsic profile of the 6.2 μm PAH feature rather than velocity shifts. As the 6.2 μm PAH traces ionised PAHs while the 11.3 μm feature traces predominantly neutral PAHs, the issues with the 6.2 μm reflect what has been found in previous studies, where AGN outflows have PAHs that are observed to be be more neutral than those in star-forming regions (O'Dowd et al. 2009; Diamond-Stanic & Rieke 2010; García-Bernete et al. 2022b,a, 2024; Rigopoulou et al. 2024; Zhang et al. 2024a; Donnelly et al. 2024; Ramos Almeida et al. 2025). Studies of the profile of the 6.2 μm PAH feature suggested that the differences in the intrinsic profile arise from the prominence of a sub-feature at ∼6.35 μm that might be due to a different molecular species (Peeters et al. 2002; Canelo et al. 2026). As we once again struggled to extract any kinematics of the 6.2 μm PAH due to differences in the intrinsic profile and its relatively low brightness compared to the 11.3 μm feature (Ramos Almeida, in prep.), this re-enforces the idea that the ionised PAHs are strongly affected in AGN outflows.

4.2. Disk subtraction

As described in Sect. 3.2, we modelled the galaxy disk velocities, fixing the orientation based on CO constraints (Ramos Almeida et al. 2022; Audibert et al. 2025). By subtracting the disk velocities from the observed 2D velocity maps presented in Fig. 3, we revealed any residual non-circular velocities that might stem from the AGN-driven outflows.

We show the disk-subtracted velocity maps for the PAH features in Figs. 6, 7, and 8 for J1509, J1430, and J1100, respectively. We focus on these three targets as they show a clear detection of kinematics in the 11.3 μm PAH feature. We measured the position angles of the outflow structures by fitting a straight line to the peak of the velocity structures, as described in the following sections. These angles are shown in Table 2.

4.2.1. J1509

J1509 is a barred spiral galaxy, and the bar and spiral arms are both detected in CO(2–1) (Ramos Almeida et al. 2022; Audibert et al. 2025). Gas outflows have been reported in low-ionisation atomic gas (Bessiere et al. 2024; Speranza et al. 2024), high-ionisation atomic and warm H_2 gas (Ramos Almeida et al. 2019), and in CO (Ramos Almeida et al. 2022; Audibert et al. 2025). The ionised outflow, traced by [OIII], [SiVI], and Paα, only shows the blueshifted component (PA ∼ −40° = 320°; Speranza et al. 2024), but the CO outflow shows blue- and redshifted emission to the north and south, respectively (Ramos Almeida et al. 2022). We summarise the orientations of the PAHs and H_2 in comparison with the literature in Table 2. The latter authors reported that because of the bar, the CO kinematics suggest a competition between inflowing and outflowing gas.

The residual velocity map of the 11.3 μm PAH for J1509 (see Fig. 6) shows clear blue- and redshifted cone structures to the north-east and south-west, respectively, and is perpendicular to the bar (as traced by the CO emission) in the inner regions of the galaxy. We measure the position angle of this structure to be 232° towards the redshifted side, where 0° is north, and the position angle increases to the east (left). A similar structure can also be seen in the H_2 S(1) line, also perpendicular to the bar, as shown in Fig. 6. This appears at a slightly different position angle of 206°, however. We show these angles in Fig. 6 and Table 2. The H_2 S(3) line also shows this structure, with a position angle closer to the PAHs than the S(1) line. The bar can also be seen in the disk-subtracted velocity of the S(3) line.

We thus detect non-circular motions related to an outflow that is present in the dust and molecular gas phase, but it is not seen in either of the velocity maps of the ionised gas from [NeII] and [NeV]. Nevertheless, as mentioned in Sect. 4.1, we indicate the outflow in the velocity dispersion of [NeV], which we show in Fig. 5. We find that the outflow regions to the north and south show a significantly higher velocity dispersion than the galaxy disk. This suggests that the ionised gas is heavily disrupted by the outflow, making its signal in the velocity maps derived from PCA decomposition weak but apparent in the velocity dispersion map.

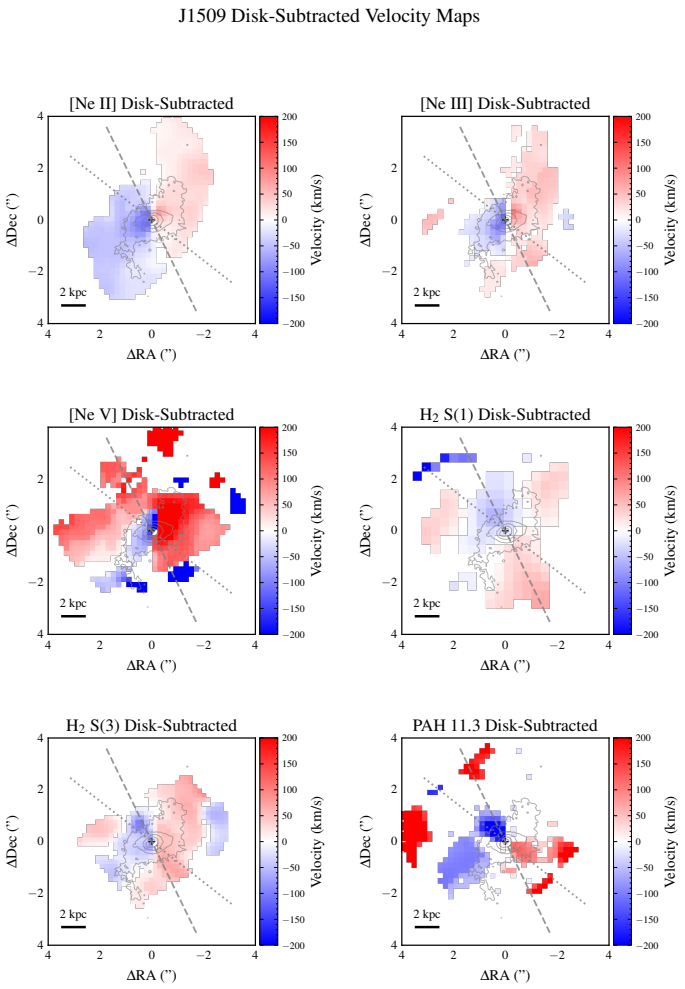


Fig. 6. Velocity maps for J1509 after subtracting a disk model. The original velocity maps are shown in Fig. 3. The grey contours show the CO(2–1) moment 0 map from Ramos Almeida et al. (2022). We show the measured position angle of the H_2 outflow with the dashed grey line, and the position angle of the PAH outflow is shown with the dotted line. We only show spaxels where the velocity is $>1\sigma$, where σ is the error in the velocity.

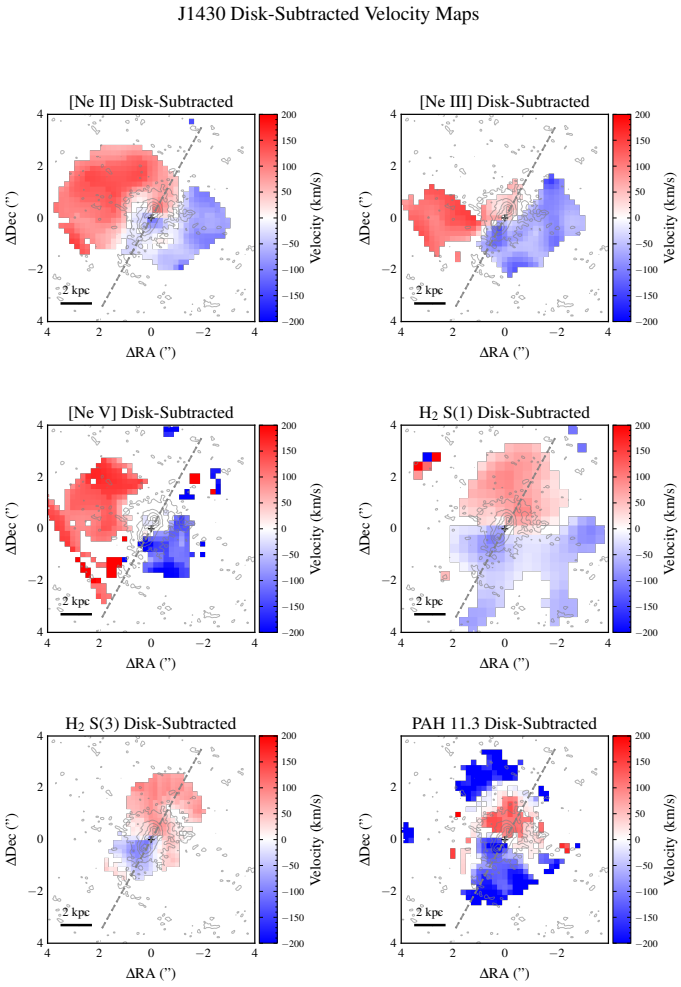


Fig. 7. Same as Fig. 6 but for J1430. Here, the position angle of the PAH and H_2 outflows match, and a single dashed line is therefore plotted to show this direction.

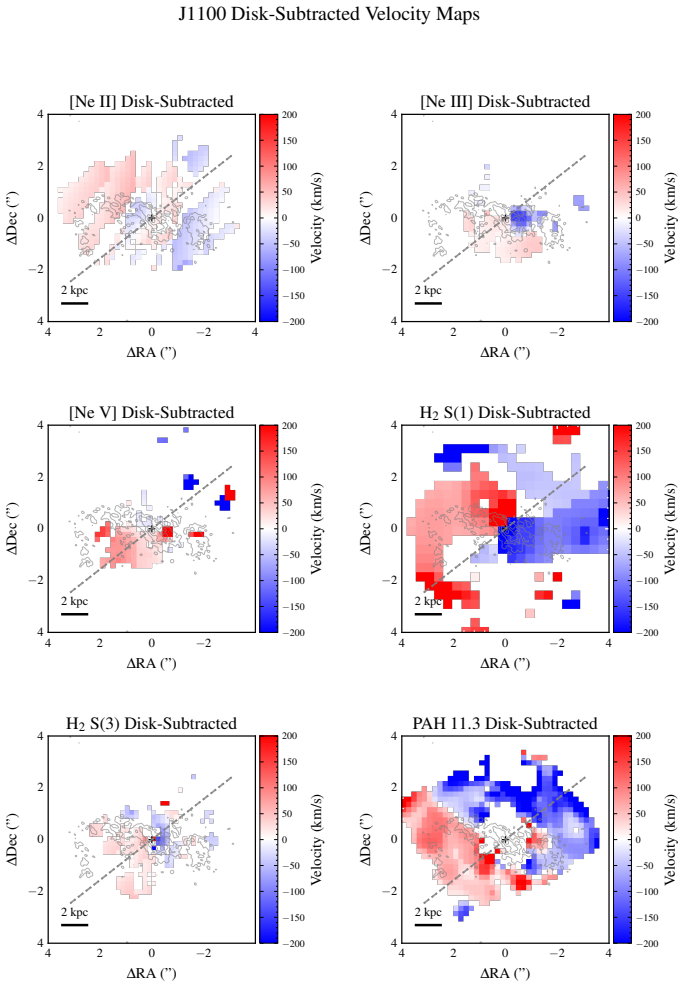


Fig. 8. Same as Fig. 6 but for J1100. Here, the position angle of the PAH and H_2 outflows match, and a single dashed line is therefore plotted to show this direction.

In addition to the potential outflow seen in the 11.3 μm PAH, H_2 S(1), and H_2 S(3) lines, Fig. 6 shows red- and blueshifted structure to the north-west and south-east, respectively, in the H_2 residual velocity map and tentatively in the PAH residual velocity map. These residuals are consistent with the ionised gas kinematics as traced by [NeII] and [NeV] and also with the spiral arms detected in CO (see Fig. 13 in Ramos Almeida et al. 2022). Because these velocity structures are consistent with the spiral arms, we suggest that they trace an inflow to the nucleus. Moreover, the spiral arm regions show the lowest velocity dispersion in the ionised gas, as shown in Fig. 5.

4.2.2. J1430

J1430 is a post-merger galaxy with a ∼55% contribution of disk rotation in CO(2–1), and the rest is dispersion dominated (Audibert et al. 2023). For this reason, we inferred the position angle of the disk from the [NeII] velocity map, as shown in Fig. 3, of ∼27° rather than ∼3° from Audibert et al. (2025), which in the other four galaxies traces the disk very well. There are still some residuals in the disk-subtracted [NeII] velocity map, which might suggest that there is a warp in the disk where the position angle changes with radius. The disk-subtracted velocity maps are shown in Fig. 7. J1430 also has a multi-phase outflow detected in low- and high-ionisation atomic gas (Harrison et al. 2014, 2015; Ramos Almeida et al. 2017; Venturi et al. 2023; Bessiere et al. 2024; Speranza et al. 2024), warm molecular gas (Zanchettin et al. 2025), and CO (Ramos Almeida et al. 2022; Audibert et al. 2023, 2025). We show the position angles of these outflows in Table 2.

Table 2. Position angles of the PAH and H_2 outflows detected from JWST compared to the literature.

Name	PAH		H_2		[OIII]		CO	
	Red	Blue	Red	Blue	Red	Blue	Red	Blue
J1509	232°	52°	206°	26°	…	–40°	132°	–8°
J1430	–29°	151°	–29°	151°	198°	65°	–18°	188°
J1100	128°	–52°	128°	–52°	…	63°	55°	200°

Notes. Position angles are measured from north to east. [OIII] values are from Speranza et al. (2024) and CO values from Ramos Almeida et al. (2022) in the case of J1509 and from Audibert et al. (2025) for J1430 and J1100.

The residual H_2 S(1) and S(3) velocity maps in Fig. 7 shows the outflow, matching the position angle of the CO(2–1) emission (the disk PA and the outflow). We measured this position angle to be –29° to the redshifted side measured from the north.

The 11.3 μm PAH velocity map receives little contribution from the disk, with the red- and blueshifted sides of the velocity field matching that of the molecular outflow and the position angle CO(2–1) contours even without disk subtraction (see Fig. 3).

Similar to J1509, we did not detect the outflow in ionised gas using the velocity maps generated from PCA decomposition. The velocity dispersion of the ionised gas along the outflow is high, however, as shown in Fig. 5. Previous studies (Ramos Almeida et al. 2017; Speranza et al. 2024) reported the detection of an ionised outflow at a position angle ∼65°–70°, which matches the direction of a jet detected in the radio (Harrison et al. 2015). This places the ionised outflow and the jet perpendicular to the outflow seen in the molecular gas and the PAHs, where Audibert et al. (2023) suggested that the jet inflates bubbles of molecular gas, driving a lateral molecular outflow.

4.2.3. J1100

J1100 is a barred spiral galaxy with an apparently undisturbed morphology (Fischer et al. 2018). The disk-subtracted velocity maps are shown in Fig. 8. As in the case of J1509, the bar and the spiral arms are detected in CO (Ramos Almeida et al. 2022; Audibert et al. 2025). The bar has a radius of ∼2.5″ and PA∼85°, and it is connected with the inner part of the spiral arms (see Fig. 7 in Ramos Almeida et al. 2022). The H_2 S(1) velocity map shown in Fig. 3 resembles the morphology and kinematics of the CO(2–1). Gas outflows have been reported in ionised gas (Harrison et al. 2014; Fischer et al. 2018; Bessiere et al. 2024; Speranza et al. 2024; Ulivi et al. 2024) and in CO (Ramos Almeida et al. 2022; Audibert et al. 2025), with the latter having position angles of 200° and 55° for its blue- and redshifted sides (see Table 2).

The disk kinematics contribute little to the velocity map of the 11.3 μm PAH, where the position angle of the kinematic axis matches that of the outflow as seen by [NeV], and therefore, the presence of the dusty outflow is clear in J1100. Moreover, the kinematics of the disk-subtracted [NeIII] line matches that of [NeV]. We measured a position angle of 128° for the outflow in J1100. We note that the ionised outflow orientation measured here from the neon maps does not match that of the [OIII] outflow reported by Speranza et al. (2024), as shown in Table 2. This might be due to the limited angular resolution of the GTC/MEGARA observations of this QSO2 (full width at half maximum of ∼1.2 arcsec). VLT/MUSE observations of this target indeed show an enhancement in the velocity dispersion to the north-west (Ulivi et al. 2024 and Bianchin et al. in prep.).

The [NeII] velocity map matches that of the disk very well (as seen in Fig. 3), where the disk-subtracted map shows very little residuals with the mean residuals $\lesssim 10$ km s^{-1}.

The H_2 S(1) map is more complex, with the disk-subtracted velocity map showing multiple components. In the inner regions lies the bar, extending from the north-east to the south-west, with a position angle consistent with the CO(2–1) emission (Ramos Almeida et al. 2022; Audibert et al. 2025). The outer regions resemble the spiral arms seen in CO. There might also be an outflow contribution in the molecular gas, where the S(5) and S(3) line, as shown in Fig. 3, shows a velocity map more consistent with [NeV]. The increase in the contribution of the outflow in the higher J H_2 lines suggests that the molecular gas is hot in the outflow (e.g. Davies et al. 2024), appearing in the higher J rotational transitions of H_2.

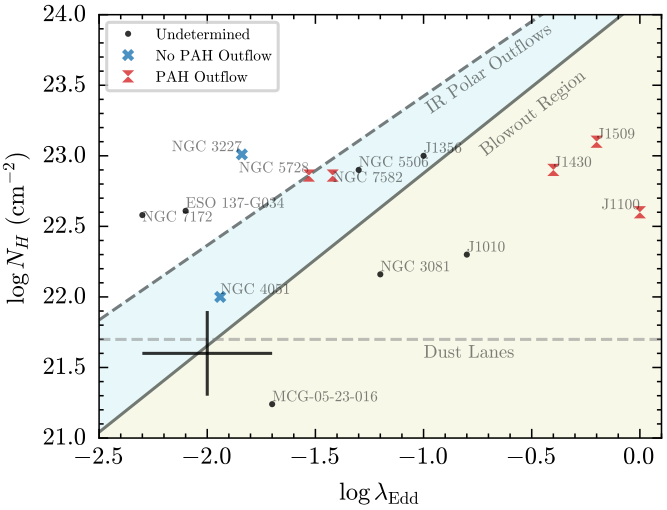


Fig. 9. Diagram of the column density, N_H, vs. the Eddington ratio, λ_{Edd} of the five QSO2s in this work and the Seyfert galaxies in Donnan et al. (2026). The sources for which we detect outflowing PAHs are shown with the red hourglass marker, and sources for which we find no dusty outflows via PAH kinematics are shown with the blue cross. The sources for which this was neither confirmed nor ruled out are shown with the black dots. We show the IR polar outflow region from Venanzi et al. (2020) as well as the blowout region from Fabian et al. (2008), where we theoretically expect dusty polar outflows. At column densities $< 5 \times 10^{21}$ cm^{-1}, dust lanes can cause the obscuration (Fabian et al. 2006; Ricci et al. 2017), which we show with the horizontal dashed grey line.

5. Discussion

5.1. How common are dusty outflows

We found evidence of PAHs in the outflow of three out of the five QSO2s in our sample. Moreover, out of those that actually show PAH kinematics, we detected kinematics consistent with an outflow in all three. The signal-to-noise ratio of the remaining two objects, J1356 and J1010, is insufficient to produce PAH velocity maps (see Fig. 3). For the case of J1356, this may be because this system is a major merger, and thus, the kinematics are simply too complex to show a coherent velocity map, while J1010 shows very little PAH emission, however.

Donnan et al. (2026) found two objects with PAH kinematic detections of the outflow in a sample of Seyfert galaxies. The full sample included ten objects, but no PAHs were determined in the outflows for five objects for a multitude of reasons. Some the galaxies were edge-on, and thus, the projected outflow velocities were extremely low simply due to orientation, and therefore could not be detected. The signal-to-noise ratio of other objects was insufficient to produce PAH velocity maps, similar to J1356 and J1010. Therefore, two out of five Seyfert galaxies showed PAH outflow kinematics. Moreover, the three objects for which PAH outflow kinematics were ruled out had lower Eddington ratios than the two that showed PAH outflow kinematics.

The potential dependence of dusty outflows on the Eddington ratio was predicted by Fabian et al. (2008), where the position of the object in a plot of the column density, N_H, versus Eddington ratio, λ_{Edd}, indicates when a dusty outflow is expected. We show this in Fig. 9.

The column densities were calculated from CO observations (García-Burillo et al. 2024) assuming Milky Way values of α_{CO} and CO ratio scaling factors derived from high-resolution data of NGC 1068 (García-Burillo et al. 2014; Viti et al. 2014). Due

to the assumptions for this calculation and the determination of the Eddington ratio, we show a large error range displayed in Fig. 9. As NGC 4051 lacks CO data, we instead used the X-ray measured column density from Pounds et al. (2004). The final source from Donnan et al. (2026) that is missing from this plot is ESO 420-G013, which lacks any reliable column density or Eddington ratios measured in the literature. However, this is one of the sources for which a dusty outflow was ruled out after no evidence of the outflow in the 11.3 μm PAH velocity map was detected.

While the sample size is small, Fig. 9 shows that all the sources with dusty outflows (red hourglass marker) tend to have higher Eddington ratios than the two sources for which dusty outflows were ruled out, namely NGC 4051 and NGC 3227 (blue cross marker). The remaining sources we designate as unknown, either due to a lack of signal-to-noise ratio or projection effects, where the outflow was edge-on, and thus, the velocity component could not be measured.

All the sources for which dusty outflows were observed appear in either the IR polar outflow region from Venanzi et al. (2020) or in the blowout region from Fabian et al. (2008) in the parameter space, where dusty outflows are theoretically expected. As previously reported by Ramos Almeida et al. (2026), the five QSO2s are in either the IR polar outflow or blowout region in Fig. 9, and the nuclear infrared spectrum of J1010 was successfully reproduced with the CAT3D-wind torus model of Hönig & Kishimoto (2017). It is therefore very likely that the five QSO2s have dusty outflows, but the current JWST observations do not allow us to detect PAH kinematics in J1010 and J1356, as previously mentioned. We also note that one of the sources for which dusty outflows were ruled out, NGC 4051, appears in the IR polar outflow region, but its column density is more uncertain due to the reasoning above.

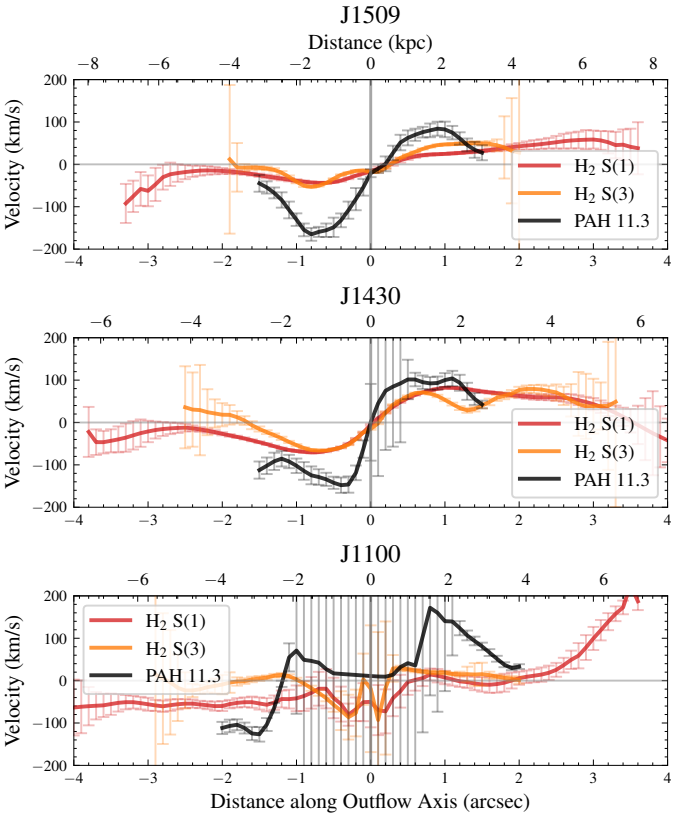


Fig. 10. Velocity profiles of the 11.3 μm PAH, H_2 S(3), and H_2 S(1) line along the outflow axis for J1509, J1430, and J1100. The profiles were extracted from the disk-subtracted maps. The top axes show the distance in kpc.

5.2. Acceleration of dust grains

To investigate the mechanisms behind the different phases of the outflow, we extracted the velocity profile along the outflow axis for the 11.3 μm PAH, the H_2 S(3), and H_2 S(1) features from the disk subtracted velocity maps, through an aperture of 1 arcsecond in increments of 0.1 arcsecond. This is shown in Fig. 10.

The 11.3 μm PAH shows a higher acceleration and then higher deceleration than the H_2 S(1) and S(3) lines. Moreover, the PAHs reach a higher peak velocity before decelerating. This matches what was observed in Seyfert galaxies in Donnan et al. (2026), although it is worth noting that the spatial scales are greater here. The peak velocity is reached at ∼1–2 kpc, while the outflows detected in Donnan et al. (2026) are on sub-kiloparsec scales. This likely reflects the higher luminosity of the targets in this work, which are known to drive larger outflows than lower-luminosity AGN (e.g. Kang & Woo 2018; Kakkad et al. 2022; Kim et al. 2023; Harrison & Ramos Almeida 2024).

One interpretation of the higher acceleration is that PAH grains are easier to accelerate due to their larger absorption cross-section relative to mass compared to H_2, which leads to a stronger radiative acceleration for the PAHs (e.g. Tielens 2010). Similarly, PAH molecules might also decelerate faster when the outflow sweeps up material in the circumnuclear environment because PAHs have a large geometric cross-section per mass. This scenario implies a decoupling of the PAHs from the molecular gas that is difficult to explain considering that the timescale on which the PAHs equilibrate with the gas (e.g. Li & Draine 2001) is much lower than the outflow timescale of ∼10^6 yr. Perhaps the molecular gas coupled to the PAHs simply does not emit.

Shocks can also play a role in these outflows as they are thought to destroy PAHs when they reach $\gtrsim$ 100 km s^{-1}, and so only slowly moving PAHs can survive (e.g. Micelotta et al. 2010). This might explain why we observe no PAHs exceeding $\gtrsim$100 km s^{-1}, although a more thorough analysis is needed to determine the presence of shocks.

This result suggests that the dusty outflow phase of AGN outflows might be short lived, where either the grains decelerate or are destroyed before the molecular or ionised gas. If they do indeed decelerate, they may fall back towards the AGN. This scenario has been postulated by Wada (2012), who proposed a fountain model in which dust grains that fail to be ejected fall back towards the AGN. The authors further suggested that the dusty torus itself is the product of these failed winds. We cannot conclusively confirm this here, but the fountain-model scenario is consistent with our observations.

6. Conclusions

We have applied PCA tomography to measure the kinematics of PAHs in five QSO2s. Three out of the five objects show a clear detection of kinematics in the 11.3 μm PAH feature, namely J1509, J1430 and J1100. Our main findings are listed below:

– In the QSO2s, high-ionisation lines of [NeV] and [NeVI] trace gas rotation in all cases except J1100, unlike in Seyfert galaxies, where they trace outflowing gas. This is likely due

to the higher AGN luminosities of the quasars, which photoionise the bulk of the gas in the galaxy disks;
- We observed two structures in the 11.3 μm PAH velocity map for J1509, particularly after subtracting the disk kinematics. An inflow structure is coincident with spiral arms, and this was also detected in molecular and ionised gas via the H_2 S(1) and [NeII] lines, respectively. Clear outflow kinematics are also clear in the 11.3 μm PAH, which is also present in the kinematics of the H_2 S(1) line and a region of high velocity dispersion in highly ionised gas in [NeV];
- In J1430, the kinematics of the 11.3 μm PAH are dominated by the outflow, which matches that of the H_2 after subtracting the disk kinematics. The outflow is consistent with the CO(2–1) emission on J1430;
- In J1100, we also see kinematic evidence of the outflow in the 11.3 μm PAH, consistent with [NeV] and the higher J H_2 S(5) and S(3) lines. The H_2 S(1) line is consistent with CO(2–1) and is dominated by the bar and innermost part of the spiral arms;
- We detected kinematic evidence of PAHs in AGN outflows in all QSO2s for which velocity maps could be constructed. This suggests that dusty outflows are more common in quasars than in Seyfert galaxies, which occupy a parameter space with higher luminosities and Eddington ratios and similar column densities than Seyfert galaxies;
- As with the Seyfert galaxies, the orientation of the PAH outflows matches that of the molecular gas, although the velocities are different;
- The acceleration of the PAHs in the outflow is higher than the molecular gas outflows, consistent with what was seen in the Seyfert galaxies. This might reflect the higher ratio of the surface area to mass of PAHs and/or dust grains compared to H_2, making them easier to radiatively accelerate by UV photons.

This work, combined with the lower luminosity sample presented in Donnan et al. (2026), shows that dusty outflows may be common in AGN with high Eddington ratios. Therefore, dusty outflows are a viable mechanism for AGN to clear their dust, potentially moving from dust-obscured phases such as hot dust-obscured galaxies to low-dust AGN such as little red dots in the high-redshift Universe.

Acknowledgements. We thank the referee for their feedback and review of the paper. F.R.D. and K.S. acknowledges funding support from grant JWST-GO-05279.002. C.R.A., A.A., and M.B. thank the Agencia Estatal de Investigación of the Ministerio de Ciencia, Innovación y Universidades (MCIU/AEI) under the grant "Tracking active galactic nuclei feedback from parsec to kiloparsec scales", with reference PID2022-141105NB-I00 and the European Regional Development Fund (ERDF). O.G.-M. acknowledges the support received by the UNAM DGAPA-PAPIIT project IN109123, SEHCITI Ciencia de Frontera project CF-2023-G100, and UNAM DGAPA sabbatical grants. MPS acknowledges support from grants RYC2021-033094-I, CNS2023-145506, and PID2023-146667NB-I00 funded by MCIN/AEI/10.13039/501100011033 and the European Union NextGenerationEU/PRTR. IGB is supported by the Programa Atracción de Talento Investigador "César Nombela" via grant 2023-T1/TEC-29030 funded by the Community of Madrid, and acknowledges support from the research project PID2024-159902NA-I00 funded by the Spanish Ministry of Science and Innovation/State Agency of Research (MCIN/AEI/10.13039/501100011033) and FSE+. M.B. acknowledges support from the Juan de La Cierva scholarship with reference JDC2023-052684-I, funded by MICIU/AEI/10.13039/501100011033 and FSE+.

References

Alonso-Herrero, A., Ramos Almeida, C., Esquej, P., et al. 2014, MNRAS, 443, 2766
Arakawa, N., Fabian, A. C., Ferland, G. J., & Ishibashi, W. 2022, MNRAS, 517, 5069
Armus, L., Charmandaris, V., Bernard-Salas, J., et al. 2007, ApJ, 656, 148
Asmus, D. 2019, MNRAS, 489, 2177
Asmus, D., Hönig, S. F., Gandhi, P., Smette, A., & Duschl, W. J. 2014, MNRAS, 439, 1648
Asmus, D., Hönig, S. F., & Gandhi, P. 2016, ApJ, 822, 109
Audibert, A., Ramos Almeida, C., García-Burillo, S., et al. 2023, A&A, 671, L12
Audibert, A., Ramos Almeida, C., García-Burillo, S., et al. 2025, A&A, 699, A83
Barro, G., Perez-Gonzalez, P. G., Kocevski, D., et al. 2025, arXiv e-prints [arXiv:2512.15853]
Bessiere, P. S., Ramos Almeida, C., Holden, L. R., Tadhunter, C. N., & Canalizo, G. 2024, A&A, 689, A271
Bianchin, M., Ramos Almeida, C., González-Martín, O., et al. 2026, A&A, 709, L9
Bock, J. J., Neugebauer, G., Matthews, K., et al. 2000, AJ, 120, 2904
Boorman, P. G., Gandhi, P., Buchner, J., et al. 2025, ApJ, 978, 118
Braatz, J. A., Wilson, A. S., Gezari, D. Y., Varosi, F., & Beichman, C. A. 1993, ApJ, 409, L5
Bushouse, H., Eisenhamer, J., Dencheva, N., et al. 2024, https://doi.org/10.5281/zenodo.10870758
Campbell, S., Rosario, D. J., Haidar, H., et al. 2025, MNRAS, 544, 648
Candian, A., & Sarre, P. J. 2015, MNRAS, 448, 2960
Canelo, C. M., Sales, D. A., Avelaneda, V. N., et al. 2026, ApJ, 1000, 171
Casey, C. M., Akins, H. B., Kokorev, V., et al. 2024, ApJ, 975, L4
Chen, K., Li, Z., Inayoshi, K., & Ho, L. C. 2025, ApJ, 994, L42
Davies, R., Shimizu, T., Pereira-Santaella, M., et al. 2024, A&A, 689, A263
Delvecchio, I., Daddi, E., Magnelli, B., et al. 2025, A&A, 704, A313
Diamond-Stanic, A. M., & Rieke, G. H. 2010, ApJ, 724, 140
Diaz-Santos, T., Lai, T. S.-Y., Finnerty, L., et al. 2025, CAFE: Continuum And Feature Extraction tool, Astrophysics Source Code Library, [record ascl:2501.001]
Donnan, F. R., García-Bernete, I., Rigopoulou, D., et al. 2024a, MNRAS
Donnan, F. R., Rigopoulou, D., & García-Bernete, I. 2024b, MNRAS, 532, L75
Donnan, F. R., García-Bernete, I., Rigopoulou, D., et al. 2026, arXiv e-prints [arXiv:2603.12200]
Donnelly, G. P., Smith, J. D. T., Draine, B. T., et al. 2024, ApJ, 965, 75
Draine, B. T., & Li, A. 2007, ApJ, 657, 810
Fabian, A. C., Celotti, A., & Erlund, M. C. 2006, MNRAS, 373, L16
Fabian, A. C., Vasudevan, R. V., & Gandhi, P. 2008, MNRAS, 385, L43
Fischer, T. C., Kraemer, S. B., Schmitt, H. R., et al. 2018, ApJ, 856, 102
Gámez Rosas, V., Isbell, J. W., Jaffe, W., et al. 2022, Nature, 602, 403
García-Bernete, I., Ramos Almeida, C., Acosta-Pulido, J. A., et al. 2016, MNRAS, 463, 3531
García-Bernete, I., Rigopoulou, D., Alonso-Herrero, A., et al. 2022a, A&A, 666, L5
García-Bernete, I., Rigopoulou, D., Alonso-Herrero, A., et al. 2022b, MNRAS, 509, 4256
García-Bernete, I., Rigopoulou, D., Donnan, F. R., et al. 2024, A&A, 691, A162
García-Burillo, S., Combes, F., Usero, A., et al. 2014, A&A, 567, A125
García-Burillo, S., Hicks, E. K. S., Alonso-Herrero, A., et al. 2024, A&A, 689, A347
González-Martín, O., Díaz-González, D. J., Martínez-Paredes, M., et al. 2025, MNRAS, 539, 2158
Haidar, H., Rosario, D. J., Alonso-Herrero, A., et al. 2024, MNRAS, 532, 4645
Haidar, H., Rosario, D. J., García-Bernete, I., et al. 2026, arXiv e-prints [arXiv:2601.02865]
Harrison, C. M., & Ramos Almeida, C. 2024, Galaxies, 12, 17
Harrison, C. M., Alexander, D. M., Mullaney, J. R., & Swinbank, A. M. 2014, MNRAS, 441, 3306
Harrison, C. M., Thomson, A. P., Alexander, D. M., et al. 2015, ApJ, 800, 45
Heckman, T. M., & Best, P. N. 2014, ARA&A, 52, 589
Hermosa Muñoz, L., Alonso-Herrero, A., Pereira-Santaella, M., et al. 2024, A&A, 690, A350
Hickox, R. C., & Alexander, D. M. 2018, ARA&A, 56, 625
Hönig, S. F., & Kishimoto, M. 2017, ApJ, 838, L20
Hönig, S. F., Kishimoto, M., Antonucci, R., et al. 2012, ApJ, 755, 149
Hönig, S. F., Kishimoto, M., Tristram, K. R. W., et al. 2013, ApJ, 771, 87
Hopkins, P. F., Hernquist, L., Cox, T. J., & Kereš, D. 2008, ApJS, 175, 356
Hviding, R. E., de Graaff, A., Miller, T. B., et al. 2025, A&A, 702, A57
Isbell, J. W., Meisenheimer, K., Pott, J.-U., et al. 2022, A&A, 663, A35
Ishibashi, W., & Fabian, A. C. 2018, MNRAS, 481, 4522
Kakkad, D., Sani, E., Rojas, A. F., et al. 2022, MNRAS, 511, 2105
Kang, D., & Woo, J.-H. 2018, ApJ, 864, 124
Kim, C., Woo, J.-H., Luo, R., et al. 2023, ApJ, 958, 145
Kocevski, D. D., Finkelstein, S. L., Barro, G., et al. 2025, ApJ, 986, 126
Kong, M., & Ho, L. C. 2018, ApJ, 859, 116
Kormendy, J., & Ho, L. C. 2013, ARA&A, 51, 511

Lai, T. S. Y., Armus, L., Bianchin, M., et al. 2023, arXiv e-prints [arXiv:2307.15169]
Leftley, J. H., Tristram, K. R. W., Hönig, S. F., et al. 2018, ApJ, 862, 17
Li, A. 2020, Nat. Astron., 4, 339
Li, A., & Draine, B. T. 2001, ApJ, 554, 778
López-Gonzaga, N., Jaffe, W., Burtscher, L., Tristram, K. R. W., & Meisenheimer, K. 2014, A&A, 565, A71
López-Gonzaga, N., Burtscher, L., Tristram, K. R. W., Meisenheimer, K., & Schartmann, M. 2016, A&A, 591, A47
Marshall, J. A., Herter, T. L., Armus, L., et al. 2007, ApJ, 670, 129
Matthee, J., Naidu, R. P., Brammer, G., et al. 2024, ApJ, 963, 129
Matthee, J., Torralba, A., Pezzulli, G., et al. 2026, A&A, submitted [arXiv:2603.17667]
Micelotta, E. R., Jones, A. P., & Tielens, A. G. G. M. 2010, A&A, 510, A36
Mingozzi, M., Cresci, G., Venturi, G., et al. 2019, A&A, 622, A146
O'Dowd, M. J., Schiminovich, D., Johnson, B. D., et al. 2009, ApJ, 705, 885
Packham, C., Radomski, J. T., Roche, P. F., et al. 2005, ApJ, 618, L17
Peeters, E., Hony, S., Van Kerckhoven, C., et al. 2002, A&A, 390, 1089
Pérez-González, P. G., Barro, G., Carniani, S., et al. 2026, arXiv e-prints [arXiv:2602.20247]
Phan, D., Pradhan, N., & Jankowiak, M. 2019, arXiv e-prints [arXiv:1912.11554]
Pierce, J. C. S., Tadhunter, C., Ramos Almeida, C., et al. 2023, MNRAS, 522, 1736
Pounds, K. A., Reeves, J. N., King, A. R., & Page, K. L. 2004, MNRAS, 350, 10
Raban, D., Jaffe, W., Röttgering, H., Meisenheimer, K., & Tristram, K. R. W. 2009, MNRAS, 394, 1325
Radomski, J. T., Packham, C., Levenson, N. A., et al. 2008, ApJ, 681, 141
Radomski, J. T., Piña, R. K., Packham, C., Telesco, C. M., & Tadhunter, C. N. 2002, ApJ, 566, 675
Ramos Almeida, C., & Ricci, C. 2017, Nat. Astron., 1, 679
Ramos Almeida, C., Alonso-Herrero, A., Levenson, N. A., et al. 2014, MNRAS, 439, 3847
Ramos Almeida, C., Piqueras López, J., Villar-Martín, M., & Bessiere, P. S. 2017, MNRAS, 470, 964
Ramos Almeida, C., Acosta-Pulido, J. A., Tadhunter, C. N., et al. 2019, MNRAS, 487, L18
Ramos Almeida, C., Bischetti, M., García-Burillo, S., et al. 2022, A&A, 658, A155
Ramos Almeida, C., Esparza-Arredondo, D., González-Martín, O., et al. 2023, A&A, 669, L5
Ramos Almeida, C., García-Bernete, I., Pereira-Santaella, M., et al. 2025, A&A, 698, A194
Ramos Almeida, C., Asensio Ramos, A., Westerdorp Plaza, C., et al. 2026, A&A, 706, A100
Reunanen, J., Prieto, M. A., & Siebenmorgen, R. 2010, MNRAS, 402, 879
Ricci, C., Trakhtenbrot, B., Koss, M. J., et al. 2017, Nature, 549, 488
Ricci, C., Ananna, T. T., Temple, M. J., et al. 2022, ApJ, 938, 67
Rigopoulou, D., Donnan, F. R., García-Bernete, I., et al. 2024, MNRAS, 532, 1598
Rusakov, V., Watson, D., Nikopoulos, G. P., et al. 2026, Nature, 649, 574
Sanders, D. B., Soifer, B. T., Elias, J. H., Neugebauer, G., & Matthews, K. 1988, ApJ, 328, L35
Shannon, M. J., & Boersma, C. 2019, ApJ, 871, 124
Siebenmorgen, R., Krügel, E., & Spoon, H. W. W. 2004, A&A, 414, 123
Smith, J. D. T., Draine, B. T., Dale, D. A., et al. 2007, ApJ, 656, 770
Speranza, G., Ramos Almeida, C., Acosta-Pulido, J. A., et al. 2024, A&A, 681, A63
Spoon, H. W. W., Marshall, J. A., Houck, J. R., et al. 2007, ApJ, 654, L49
Stalevski, M., Asmus, D., & Tristram, K. R. W. 2017, MNRAS, 472, 3854
Steiner, J. E., Menezes, R. B., Ricci, T. V., & Oliveira, A. S. 2009, MNRAS, 395, 64
Tielens, A. G. G. M. 2008, ARA&A, 46, 289
Tielens, A. G. G. M. 2010, The Physics and Chemistry of the Interstellar Medium
Tristram, K. R. W., Burtscher, L., Jaffe, W., et al. 2014, A&A, 563, A82
Ulivi, L., Venturi, G., Cresci, G., et al. 2024, A&A, 685, A122
Veenema, O., Thatte, N., Rigopoulou, D., et al. 2025, MNRAS, 544, 3361
Veenema, O., Thatte, N., Rigopoulou, D., et al. 2026, MNRAS, 548, stag785
Venanzi, M., Hönig, S., & Williamson, D. 2020, ApJ, 900, 174
Venturi, G., Treister, E., Finlez, C., et al. 2023, A&A, 678, A127
Viti, S., García-Burillo, S., Fuente, A., et al. 2014, A&A, 570, A28
Wada, K. 2012, ApJ, 758, 66
Zanchettin, M. V., Ramos Almeida, C., Audibert, A., et al. 2025, A&A, 695, A185
Zhang, L., & Ho, L. C. 2023, ApJ, 953, L9
Zhang, L., García-Bernete, I., Packham, C., et al. 2024a, ApJ, 975, L2
Zhang, L., Packham, C., Hicks, E. K. S., et al. 2024b, ApJ, 974, 195
Zhang, L., Packham, C., Hicks, E. K. S., et al. 2026, ApJ, 998, L32

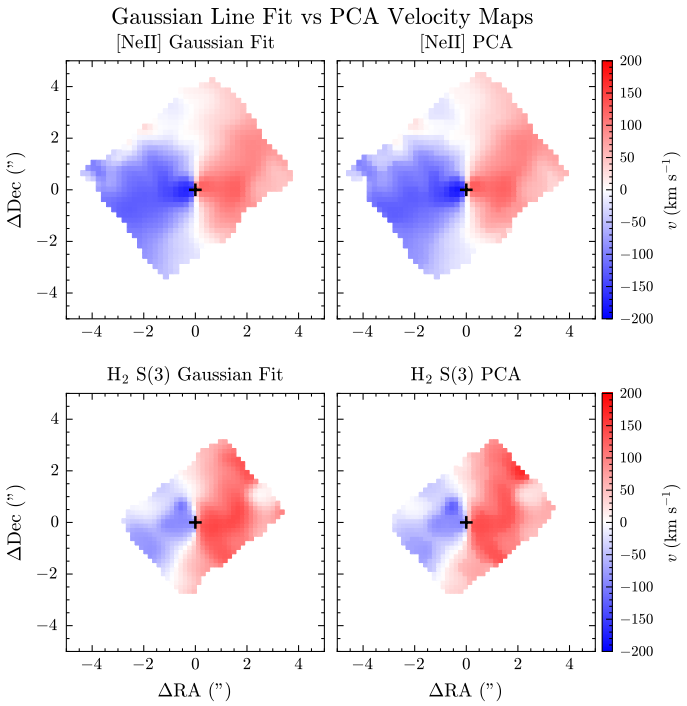


Fig. A.1: Comparison between the PCA technique and a more traditional method of producing a velocity map by fitting a Gaussian to the spectrum of each spaxel. We show this comparison for the [NeII] and H_2 S(3) line for J1509.

Appendix A: Comparison to line fitting

To verify that the PCA technique is accurate at producing velocity maps, we compare it to a more traditional method of fitting a Gaussian line profile to every spaxel for the emission lines where such traditional methods are viable. For each spaxel, we allow the amplitude, central wavelength and standard deviation of the Gaussian to vary as free parameters, where we use the central wavelength to infer the velocity.

We show a comparison in Fig. A.1 for J1509 where we show [NeII] and the H_2 S(3) line. We find that the velocities are almost identical with the PCA doing a good job at accurately inferring the velocities.

Appendix B: Continuum subtraction

To investigate the impact that our choice of continuum subtraction has on the PCA decomposition and the subsequent velocities we measure, we test different continuum subtraction methods. We use the 11.3 μm PAH feature in J1509 for this testing.

In Fig. B.1, we show different continuum subtractions and the resulting velocity maps. In particular we try a narrower wavelength range where we exclude more of the wings of the feature. We also try a wider wavelength range, where we include more of the wing on the longer wavelength side. Finally we try no continuum subtraction at all.

We find that in all cases the velocity map is broadly consistent which suggests that the continuum subtraction method does not have a large impact on the resultant velocity map. Even when the wavelength range is very narrow and the continuum subtraction removes much of the PAH emission from the wings of the feature, the core is sufficient to measure kinematics from. Therefore the continuum subtraction we have used in this work is sufficient to measure the kinematics of the 11.3 μm PAh feature.

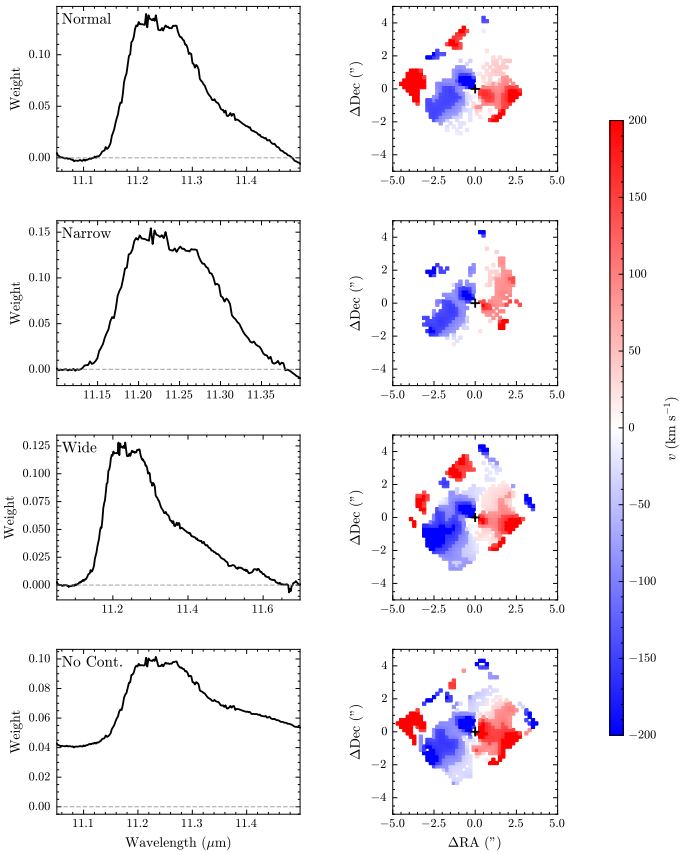


Fig. B.1: Tests of different continuum subtractions for the 11.3 μm PAH feature in J1509. *Left panels*: Eigenspectra of the first principal component. *Right panels*: Inferred velocity map from the PCA decomposition. The top panels show the continuum subtraction used in this work, while the following panels show a narrower wavelength range, a wider wavelength range, and no continuum subtraction.

We also test no continuum subtraction, where the kinematics are surprisingly well constrained. This is likely because the continuum is weak compared to the PAH feature, and the changes in the profile due to a Doppler shift still dominates the higher order principal components.